Element redistribution during early stages of oxidation in a Ni$_{38}$Cr$_{22}$Fe$_{20}$Mn$_{10}$Co$_{10}$ multi-principal element alloy

Elizabeth J. Kautz[1*], Sten V. Lambeets[2], Daniel E. Perea[2], Angela Y. Gerard[3], Junsoo Han[3], John R. Scully [3], James E. Saal[4], Daniel K. Schreiber[5*]

[1]National Security Directorate, Pacific Northwest National Laboratory, Richland, WA 99352 USA
[2]Earth and Biological Sciences Directorate, Pacific Northwest National Laboratory, Richland, WA 99352 USA
[3]Materials Science and Engineering Department, University of Virginia, Charlottesville, VA 22904
[4]Citrine Informatics, Redwood City, CA, 94063
[5]Energy and Environment Directorate, Pacific Northwest National Laboratory, Richland, WA 99352 USA
*corresponding authors: elizabeth.kautz@pnnl.gov, daniel.schreiber@pnnl.gov

1

Abstract

Element redistributions after initial oxidation of a $Ni_{38}Cr_{22}Fe_{20}Mn_{10}Co_{10}$ (at. %) multi-principle element alloy at 120 °C and 300 °C is captured via *in situ* atom probe tomography. All cations contribute to the oxide in both conditions, consisting of Cr-rich inner oxide and Fe, Mn, Co and Ni-rich outer oxide. At lower temperature, Ni tends to be trapped at the outer/inner oxide interface, while Ni enriches at the oxide/metal interface at higher temperature in tandem with Cr metal depletion. These observations confirm oxidation of complex alloys involves the formation of metastable, multi-layered oxide films, with a distinct tendency for solute trapping.

Key Words: multi principal element alloy, oxidation mechanisms, oxide/metal interface, atom probe tomography

2

An expansive composition space for alloy design has been created by the advent of multi-principal element alloys (MPEAs) [1-3]. MPEAs are typically comprised of five or more elements between 5 and 35 at. %, and are currently being considered for a wide range of structural applications due their exceptional mechanical properties, irradiation resistance, and thermodynamic stability [2]. Unique characteristics of these alloys, namely the formation of a single-phase solid solution with a low tendency for precipitation of intermetallic compounds and sluggish solid state diffusion [2], make MPEAs intriguing candidates for use in corrosive and oxidizing environments [4, 5].

Many MPEAs have demonstrated favorable corrosion characteristics, which are highly dependent on alloy composition. In conventional alloys, Cr additions (often > 11 at. %) oftentimes aid corrosion resistance, although the Cr content needed for passivation may vary for different alloy systems and environments. These critical Cr additions are responsible for the 'stainless' properties of several conventional alloys (e.g. Ni-Cr, Fe-Cr-Ni, Fe-Cr, and Ni-based super alloys) through the formation of a continuous, protective Cr-rich oxide [6-8]. Numerous MPEAs have Cr concentrations above this threshold, but the presence of several other principal alloying elements could significantly impact passivation behavior, including the critical Cr concentration for passivation, and must be considered.

Recently, oxide compositions and structures have been explored in various alloys, including the well-known Cantor alloy, a single solid solution FCC phase, equiatomic $Fe_{20}Cr_{20}Mn_{20}Ni_{20}Co_{20}$ alloy [9-14]. Oxidation of FeCrMnNiCo-containing alloys in atmospheric conditions leads to the formation of a layered oxide film, typically comprised of Cr-rich inner and Mn-rich outer oxides [11-13], primarily attributed to the outward diffusion of cations [10]. In a study by Kim *et al,* high temperature oxidation of FeCrMnNiCo (900-1100 °C in 20% O_2/80%

3

N$_2$ for 24 h) revealed the formation of an inner Cr$_2$O$_3$ and outer Mn$_2$O$_3$ oxide layers at 900 °C was accompanied by enrichment of Ni, Fe, and Co in the adjacent base alloy. At higher temperatures (1000-1100 °C), the outer oxide transformed from Mn$_2$O$_3$ to Mn$_3$O$_4$, and an intermediate (Mn,Cr)$_3$O$_4$ ternary oxide was formed, in which Ni, Fe, and Co were in solid solution [11]. The presence of Mn in particular is considered detrimental to oxidation resistance due to its high mobility and low energy of formation for several Mn oxides [12, 15, 16]. Rapid Mn transport to the oxide/metal interface can result in corresponding depletion of Mn in the base alloy, ultimately leading to formation of vacancies above saturation and subsequently pores that function as short circuit diffusion paths for ions, accelerating the oxide growth rate [11, 12]. Within the oxide, the multivalent nature of Mn could also stabilize charged defects. Together these localized regions of modified alloy and oxide chemistries may accelerate sluggish diffusivity typical in MPEAs and passive films, and thus have implications for oxidation resistance [11].

Despite several prior studies detailing compositions of oxide films and associated kinetics, results vary significantly with regard to alloy chemistry, environmental conditions, and characterization techniques used [12-14, 17-20]. Many studies have investigated (near) equiatomic alloys that may not be optimal for corrosion resistance [3]. Due to the diversity of the literature on MPEA corrosion, the composition and nature of oxide films formed on compositionally complex alloy surfaces is not well-established [4]. To gain further insight into initial stages of oxide formation in such systems, an *in situ* atom probe tomography (APT) approach was applied [21, 22] to investigate elemental redistributions accompanying oxidation in a Ni$_{38}$Cr$_{22}$Fe$_{20}$Mn$_{10}$Co$_{10}$ (at. %) alloy.

4

The $Ni_{38}Cr_{22}Fe_{20}Mn_{10}Co_{10}$ (at. %) alloy was arc melted, cast, and homogenized at 1100 °C for 96 h [23]. APT needle specimens were made using the focused ion beam lift-out method [24], then analyzed (via field evaporation) to remove Ga ion damage, exposing a pristine alloy surface for oxidation. Pristine samples were transferred under ultra-high vacuum (UHV) (10^{-7}–10^{-8} mbar) to a gas-phase reactor chamber preheated to the desired temperature, where specimens were exposed to O_2 gas (99.993% purity) at 10 mbar for 120 °C for 5 minutes and 300 °C for 2 minutes. Specimens were transferred back to the analysis chamber under UHV, where composition across the oxide/metal interface was analyzed. Pressure-temperature-time conditions were selected to develop nanoscale oxides ~2–4 nm thick. A CAMECA local electrode atom probe (LEAP) 4000X HR system operated in laser-pulsing mode was used for data collection. Data were reconstructed and analyzed using the Integrated Visualization and Analysis Software (IVAS), version 3.8.4 by CAMECA. Further details on APT analysis conditions and peak identification within the APT mass spectra are provided in Supplementary Information Figures S1-S2.

5

APT atom maps of a single specimen before and after two different oxidation exposures are shown in Figure 1. Oxidation results in a thin layer of mixed metal-oxygen ion complexes of all base alloy components within the first ~5 nm of the specimen apex. Oxidation also occurs along the sides of the specimen, but those features are outside the field of view of the APT reconstruction. Elemental and cation fractions in the base alloy oxides formed after both oxidation conditions are presented in Table 1 and compared to the nominal and APT-measured base alloy composition. Fractions of alloying elements and their cations are the focus of results presented herein, due to the known oxygen deficits in laser-assisted APT of oxide materials [25]. Results reported in Table 1 are averages and standard deviations from duplicate APT data sets, and highlight trends in elemental partitioning before/after oxidation. A significant change in the Cr atomic fraction in the base alloy (0.23) versus oxides (0.26 and 0.32 after oxidation at 120 °C and 300 °C, respectively) is measured. In contrast, Co and Fe content decrease in the oxide with increasing oxidation temperature. We also find significant Ni in the oxide ($\geq$ 0.36). Interestingly, Ni and Mn concentrations are approximately equal to their base alloy concentrations.
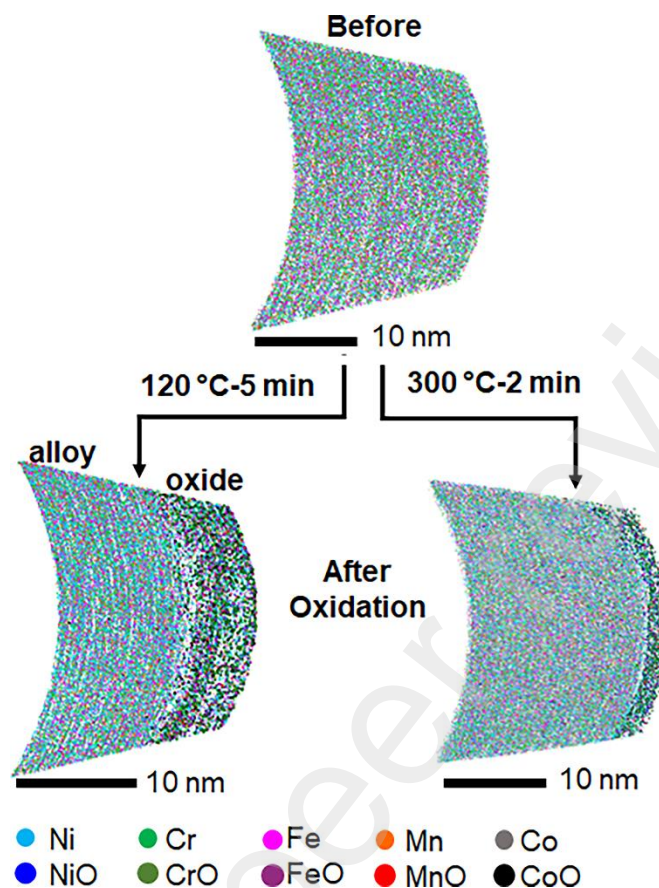
6

Figure 1. 3D ion maps of all major alloying elements (and their oxides) before and after oxidation at either 120 °C-10 mbar O_2-5 minutes or 300 °C-10 mbar O_2-2 minutes in high purity O_2 gas. APT reconstructions shown are cropped to ~10 nm thick to clearly show the oxide/metal interface.

Table 1. Summary of elemental and cation fractions for the nominal alloy composition, the APT-measured base alloy (before oxidation), and in the oxide layers formed at 120 °C-5 minutes and 300 °C-2 minutes in 10mbar O_2 gas. Fractions reported are averages and standard deviations determined from 3-4 duplicate APT needle specimens per oxidation condition. A 14 at. % O isoconcentration surface was used to delineate oxide from base alloy when quantifying the oxide composition.

	Ni	Cr	Fe	Mn	Co
Nominal	0.38	0.22	0.2	0.1	0.1
APT-measured base alloy	0.37±0.01	0.23±0.004	0.20±0.004	0.11±0.002	0.1±0.001
Oxide (120 °C)	0.37±0.01	0.26±0.004	0.19±0.01	0.10±0.004	0.08±0.001
Oxide (300 °C)	0.36±0.03	0.30±0.1	0.16±0.03	0.12±0.03	0.06±0.02

7

From Table 1, the oxide cation fractions are self-similar and comparable to elemental

fractions in the base alloy, which may be attributable to the phenomena of nonequilibrium solute

capture [26]. However, Table 1 does not detail any differences in spatial arrangement of

elements, which requires further consideration. 2D compositional contour plots were generated

from a sub-volume of APT specimens and are presented in Figure 2(a) and (b) for both oxidation

exposures, respectively. The thermal scale uses the same concentration ranges for each oxidation

condition to enable a direct visual comparison of the elemental partitioning between oxidation

conditions. After oxidation at both temperatures, Ni is present in the oxide, with slight

enrichment on the alloy side of the oxide/alloy interface. Cr enrichment is found in the inner

oxide for both 120 °C and 300 °C exposures, although to a greater extent in the oxide formed at

300 °C. Fe, Mn, and Co maps all highlight a similar trend for both temperatures of depletion in

the inner oxide. Fe, Mn, and Co are also found in the outer oxide after 120 °C oxidation,

however this trend was not observed in the contour plots for the oxide formed at 300 °C. It is

presumed that the outermost oxide was not captured in the APT reconstruction, resulting in the

absence of a clear Fe, Mn, and Co enriched outer oxide that is expected to be present.
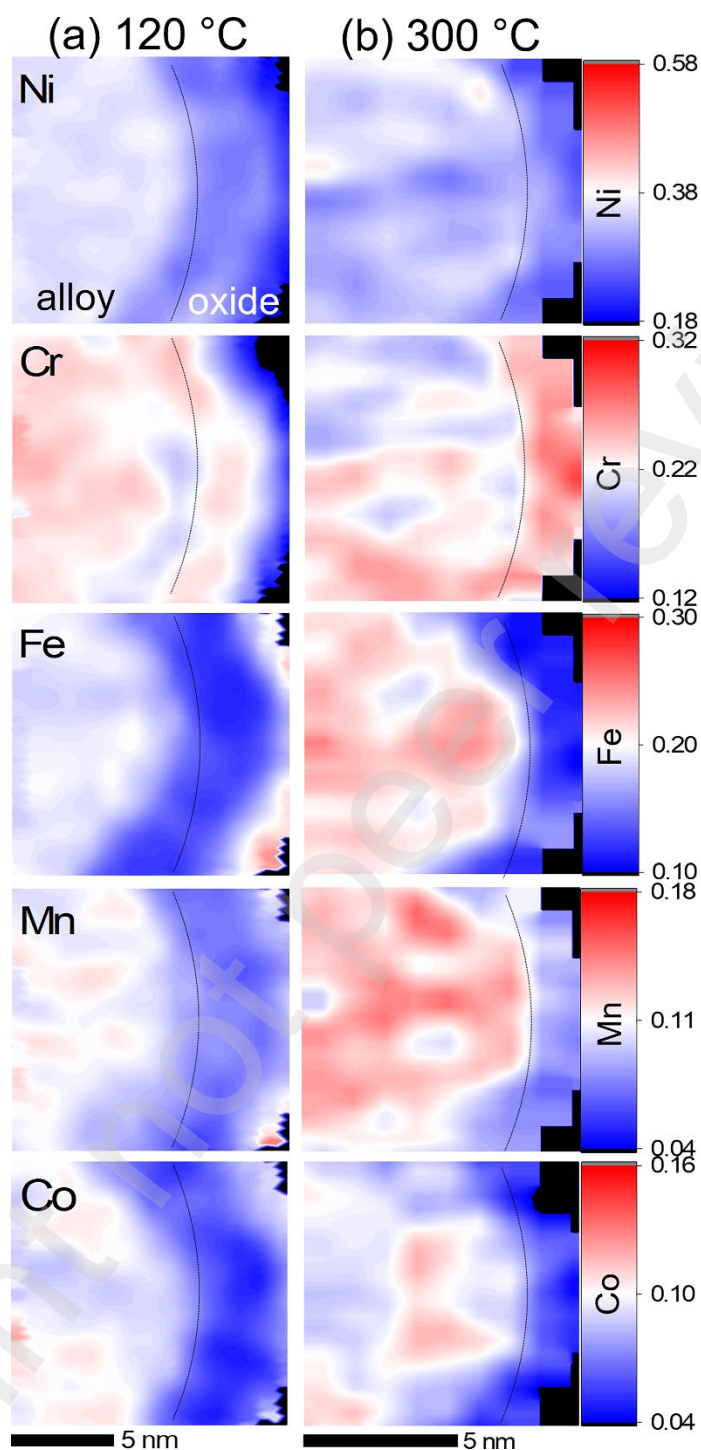
8

Figure 2. Two-dimensional compositional contour plots illustrating elemental fractions across the $Ni_{38}Fe_{20}Cr_{22}Mn_{10}Co_{10}$ alloy/oxide interface after oxidation at (a) 120°C-10 mbar-5 minutes, and (b) 300 °C-10 mbar-2 minutes. The approximate location of the oxide/metal interface is indicated by a black dashed line in each plot. Contour plots were generated from reconstructed APT data using a cubic region of interest 1 nm thick. The red/white/blue color scale indicates the composition (in elemental fraction), where black denotes a concentration below the minimum value noted of the color scale.

9

To further probe the elemental partitioning accompanying oxidation, the proximity

histogram method [27] was used to quantify local concentration across oxide/metal interfaces.

The zero position in concentration profiles indicates the approximate inflection point in the Cr

concentration curve, which is a consistent and repeatable indicator of the oxide/metal interface.

Concentration profiles given in Figure 3 provide fractions of all major alloying elements for

120 °C and 300 °C oxides, respectively. Error bars in concentration profiles represent 1σ from

standard counting error, defined as: $\sigma = \sqrt{c_i(100 - c_i)/N_T}$, where c_i is the local concentration

of species i and N_T is the total number of atoms in the concentration measurement. Results

presented here are repeatable between similar needle specimens and exposure conditions, as

shown in Supplemental Information Figure S3, which also reports as-measured oxygen

concentration for reference. Cation fractions for the 120 °C oxide show slight Ni enrichment in

the base alloy adjacent to the oxide/metal interface, followed by a decrease in Ni in the Cr-rich

inner oxide, and then an increase in Ni (referred to as Ni 'trapping', indicated by the black arrow

in Fig. 3a). Fe, Mn, and Co concentrations are depleted (relative to the base alloy) in the inner

oxide, and enriched in the outer oxide. A significant cation fraction of Ni (~0.25) is also found in

the outer oxide, where Cr fraction drops from > 0.3 in the inner oxide to < 0.1 in the outer oxide.

The profile for the oxide formed after oxidation at 300 °C-2 minutes (Figure 3 (d)) shows similar

trends in alloy element distribution. Ni is again enriched at in the base alloy adjacent to the

oxide, some Ni trapping persists in Cr-rich inner oxide and significant Ni exists in the outer

oxide. Important differences are that Ni enrichment in the base alloy is higher and peak Cr

enrichment in the inner oxide is greater after 300 °C oxidation (0.48 Ni, 0.39 Cr) versus 120 °C

(0.42 Ni, 0.32 Cr). Although a portion of the 300 °C outer oxide was lost in the destructive APT

10

analysis, the small amount of the outer oxide from which data was acquired shows a similar

trend of increasing Fe, Mn, and Co cation fractions, with significant Ni (~ 0.35) present.

Complementary visualization of the relative contribution of each alloying element to inner and

outer oxides is demonstrated in the stacked area plots given in Figure 3(c)-(d). Comparison of

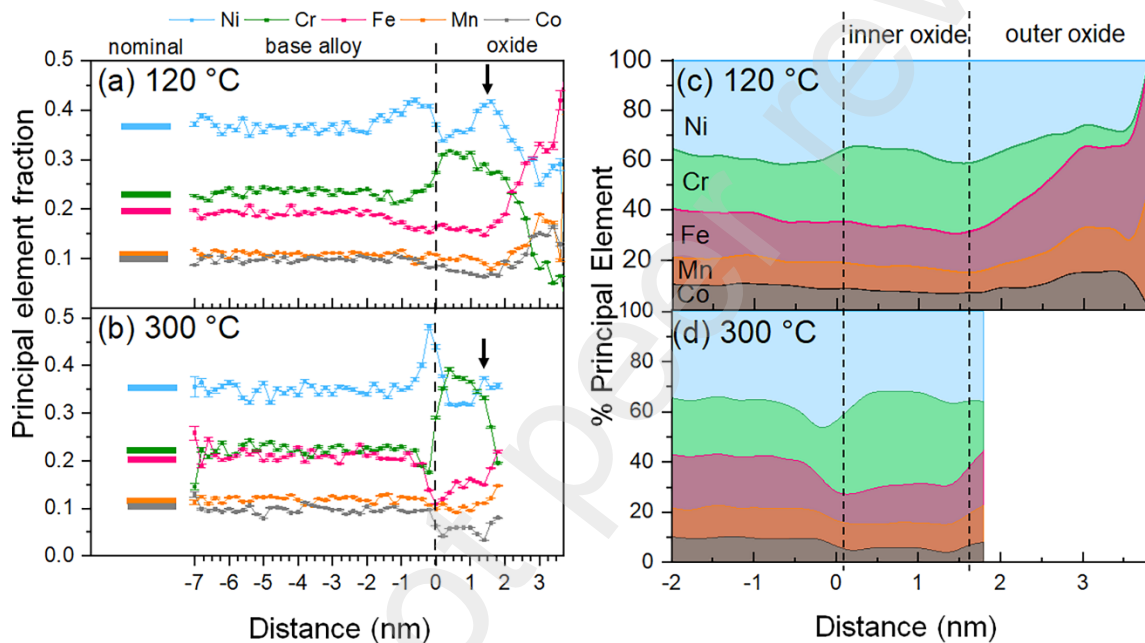Figure 3 (c) and (d) highlights that the inner oxide is more well-defined and Cr-rich with

increasing temperature.

Figure 3. Proximity histograms across the oxide/metal interface after oxidation at (a, c) 120 °C-
10 mbar-5 minutes, and (b, d) 300 °C-10 mbar-2 minutes. Fractions are provided on a scale of 0
to 1, where error bars represent 1σ from standard counting error. The zero position of the profiles
was based on the inflection point of the Cr profile. The nominal base alloy composition, as
determined by APT, is given by horizontal lines to the left of the concentration profile. Black
arrows indicate apparent Ni trapping near the inner oxide layer. Note that the 300 °C outer oxide
was not captured in the APT analysis, and hence is cut-off in sub-figures (b) and (d).

Examination of 2D contour plots and concentration profiles reveals that compositionally

layered oxide films are formed containing all alloying elements, and are comprised of two

primary layers: inner Cr-rich, and outer Fe, Ni, Mn, Co–rich oxides. Ni redistribution in the

oxide and adjacent base alloy accompanies the formation of this layered oxide. Additionally, a

11

region of Cr depletion in the metal is observed. Ni is 'trapped' in the 120 °C oxide and at the oxide/metal interface up to an atomic fraction of 0.42 (in comparison to the nominal ~0.38). After oxidation at 300 °C, Ni trapping is still present in the oxide, but a much higher Ni enrichment at the oxide/metal interface (up to 0.48) is measured. Cr enrichment and Ni depletion are observed in the inner oxide. The Cr concentration consistently drops in the outer oxide, whereas Fe, Mn, Co, and Ni content increase.

Schematics in Figure 4 highlight the initial elemental partitioning accompanying oxidation of $Ni_{38}Fe_{20}Cr_{22}Mn_{10}Co_{10}$ at 120 °C and 300 °C in 10 mbar O_2 gas compared to our prior work on aqueous corrosion of the same alloy [28]. During room temperature corrosion in an aqueous NaCl environment at pH 4 for 10 ks, the formation of a Cr-rich oxide with small amounts of Ni, Fe, and Mn are observed. One major difference is that the chemical dissolution of Ni, Fe, and Co was observed because single element and spinel type oxides containing these elements are unstable at pH 4 [28]. The presence of a Cr-rich inner oxide, with Ni, Fe, and Mn also present is consistent with our findings. However, dissolution of some elements in aqueous corrosion leads to the formation of a distinctive outer oxide layer in comparison to that formed in a dry oxidation environment.
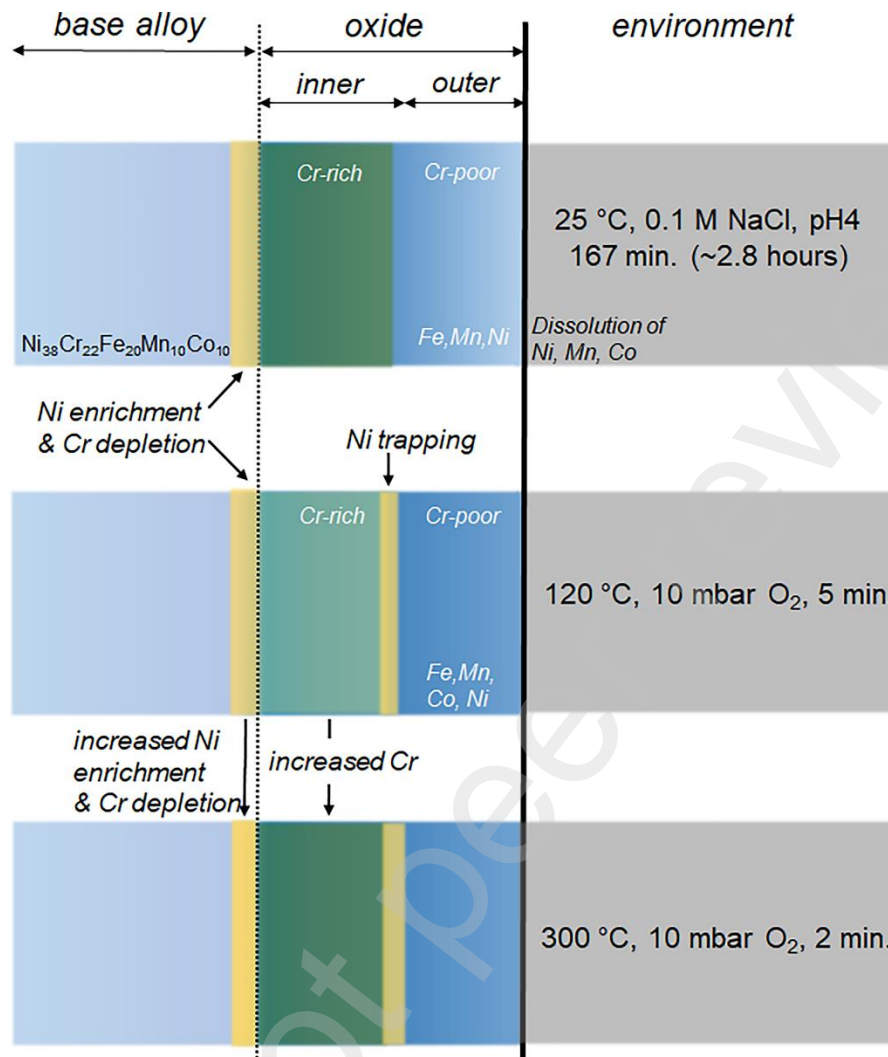
12

Figure 4. Schematic illustration of element redistribution across the base alloy/oxide metal interface for room temperature aqueous corrosion in 0.1 M NaCl (pH 40 for 10,000 seconds, or ~167 minutes) compared to dry oxidation experiments performed here (120 °C-10 mbar-5 minutes, and 300 °C-10 mbar-2 minutes). Schematics are not drawn to scale.

Thermodynamically, the oxide formed on the $Ni_{38}Fe_{20}Cr_{22}Mn_{10}Co_{10}$ MPEA is expected to consist of distinct phases, such as NiO, Cr_2O_3, Fe_2O_3, Mn_2O_3, $(Co, Fe)_2O_3$ and mixed spinels (e.g. $(NiFeMnCo)Cr_2O_4$ or $NiFe_2O_4$) [29]. Such elaborate phase separation from a complex but single phase MPEA requires significant element redistributions that are prohibitive by the short times and low temperatures used here. Hence, the initial oxide is likely a combination of metastable oxides, the formation of which is driven by both thermodynamic and kinetic (e.g.

13

mobility) factors. In particular, the diffusivity of elements in the alloy relative to their cation diffusivities in the oxide scale is critical to understanding oxide scale development [30].

Prior work studying diffusivity of alloying elements in MPEAs has established fastest to slowest diffusers (in the base alloy) are: Mn, Cr, Fe, Co, Ni [31]. However, mobility of these species in complex oxides is an important consideration that is not yet established, where diffusion of cations depends strongly on charge state and local defects, in addition to oxide structure and composition [32]. A study on aqueous corrosion of the same MPEA suggested Cr enrichment in the oxide may be attributed to faster diffusion of Cr in the base alloy in comparison to other alloying elements, and the lower free energy of formation for Cr_2O_3 versus other transition metal oxides [28]. The mismatch in element mobilities can partially explain the Cr depletion is found in the metal adjacent to the oxide/metal interface [33], but other thermodynamic factors of selective oxidation behavior likely contribute. In this work, Cr enrichment and present of all alloying elements is observed in the inner oxide, however not in sufficient amounts to support consumption of all Cr^{3+} as a mixed spinel or corundum [29]. The distinctly different outer oxide could be formed via diffusion of other alloying elements through and reaction with the Cr-rich inner oxide layer. Ni trapping in the oxide could be related to sluggish diffusivity of Ni relative to other alloying elements in the oxide, and may suggest early stages of spinel formation. In addition, morphology and presence of high diffusivity paths (e.g. pores, grain boundaries) may also influence element redistributions. The presence of nanocrystalline oxide grains formed on needle specimens [22] may facilitate local short-circuit diffusion of oxygen to the base alloy, and also the outward diffusion of cations, particularly Mn, as demonstrated in prior work on Cantor alloy [12].

14

To summarize, we measured in 3D and at the nanoscale the elemental redistributions that accompany early stages of oxidation in a non-equiatomic, single phase $Ni_{38}Fe_{20}Cr_{22}Mn_{10}Co_{10}$ (at. %) MPEA. An *in situ* APT approach was used to track changes in elemental and cation fractions in the alloy and oxide, respectively, for 120 °C-5 minute and 300 °C-2 minute exposures in 10 mbar O_2. A layered oxide film is formed for both conditions, comprised of an inner Cr-rich oxide and an outer Fe, Ni, Mn, Co, and Ni–rich oxide. At lower temperatures, stronger Ni trapping is found in the inner oxide, whereas at higher temperatures, stronger Ni-enrichment at the oxide/metal interface occurs. Neither the inner nor outer oxides can be defined as a stoichiometric oxide phase, but more likely consists of metastable oxides that have not yet reached a thermodynamically stable form. The observed Ni-enrichment in the base alloy and the formation of a layered oxide is consistent with the composition of the passive film formed on the same alloy during longer-term corrosion in an aqueous NaCl environment. Our work has implications for alloy design, in which evaluating oxidation or corrosion behavior with higher fidelity than traditional methodologies is needed.

Declaration of Competing Interest

The authors declare that they have no known competing interests.

References

[1] J.W. Yeh, S.K. Chen, S.J. Lin, J.Y. Gan, T.S. Chin, T.T. Shun, C.H. Tsau, S.Y. Chang, Advanced Engineering Materials 6(5) (2004) 299-303.

[2] D.B. Miracle, O.N. Senkov, Acta Materialia 122 (2017) 448-511.

[3] P. Lu, J.E. Saal, G.B. Olson, T. Li, O.J. Swanson, G.S. Frankel, A.Y. Gerard, K.F. Quiambao, J.R. Scully, Scripta Materialia 153 (2018) 19-22.

[4] Y. Qiu, S. Thomas, M.A. Gibson, H.L. Fraser, N. Birbilis, npj Materials Degradation 1(1) (2017) 15.

[5] A.V. Ayyagari, B. Gwalani, S. Muskeri, S. Mukherjee, R. Banerjee, npj Materials Degradation 2(1) (2018) 1-10.

[6] E. Gardin, S. Zanna, A. Seyeux, A. Allion-Maurer, P. Marcus, Corrosion Science 143 (2018) 403-413.

[7] K. Sieradzki, R.C. Newman, J. Electrochem. Soc 133(9) (1986) 1979-1980.

[8] S. Thomas, N. Birbilis, M.S. Venkatraman, I.S. Cole, Corrosion Science 69 (2013) 11-22.

[9] B. Cantor, I.T.H. Chang, P. Knight, A.J.B. Vincent, Materials Science and Engineering: A 375 (2004) 213-218.

[10] W. Kai, C.C. Li, F.P. Cheng, K.P. Chu, R.T. Huang, L.W. Tsay, J.J. Kai, Corrosion Science 108 (2016) 209-214.

[11] Y.-K. Kim, Y.-A. Joo, H.S. Kim, K.-A. Lee, Intermetallics 98 (2018) 45-53.

[12] G. Laplanche, U. Volkert, G. Eggeler, E. George, Oxidation of Metals 85(5-6) (2016) 629-645.

16

[13] G.R. Holcomb, J. Tylczak, C. Carney, JOM 67(10) (2015) 2326-2339.

[14] T.M. Butler, M.L. Weaver, Journal of Alloys and Compounds 674 (2016) 229-244.

[15] R.K. Wild, Corrosion Science 17(2) (1977) 87-104.

[16] F.H. Stott, F.I. Wei, C.A. Enahoro, Materials and Corrosion 40(4) (1989) 198-205.

[17] W. Kai, C.C. Li, F.P. Cheng, K.P. Chu, R.T. Huang, L.W. Tsay, J.J. Kai, Corrosion Science 121 (2017) 116-125.

[18] S. Xia, C.M. Lousada, H. Mao, A.C. Maier, P.A. Korzhavyi, R. Sandström, Y. Wang, Y. Zhang, Frontiers in Materials 5 (2018) 53.

[19] H.S. Grewal, R.M. Sanjiv, H.S. Arora, R. Kumar, A. Ayyagari, S. Mukherjee, H. Singh, Advanced Engineering Materials 19(11) (2017) 1700182.

[20] Y. Qiu, S. Thomas, M.A. Gibson, H.L. Fraser, K. Pohl, N. Birbilis, Corrosion Science 133 (2018) 386-396.

[21] S.V. Lambeets, T. Visart de Bocarmé, D.E. Perea, N. Kruse, The Journal of Physical Chemistry Letters 11(8) (2020) 3144-3151.

[22] E.J. Kautz, B. Gwalani, S.V.M. Lambeets, L. Kovarik, D.K. Schreiber, D.E. Perea, D. Senor, Y.-S. Liu, A.K. Battu, K.-P. Tseng, S. Thevuthasan, A. Devaraj, under review (2020).

[23] P. Lu, J.E. Saal, G.B. Olson, T. Li, S. Sahu, O.J. Swanson, G.S. Frankel, A.Y. Gerard, J.R. Scully, Scripta Materialia 172 (2019) 12-16.

[24] K. Thompson, D. Lawrence, D.J. Larson, J.D. Olson, T.F. Kelly, B. Gorman, Ultramicroscopy 107(2) (2007) 131-139.

[25] B. Gault, D.W. Saxey, M.W. Ashton, S.B. Sinnott, A.N. Chiaramonti, M.P. Moody, D.K. Schreiber, New Journal of Physics 18(3) (2016) 033031.

17

[26] X.-x. Yu, A. Gulec, Q. Sherman, K.L. Cwalina, J.R. Scully, J.H. Perepezko, P.W. Voorhees, L.D. Marks, Physical Review Letters 121(14) (2018) 145701.

[27] O.C. Hellman, J.A. Vandenbroucke, J. Rüsing, D. Isheim, D.N. Seidman, Microscopy and Microanalysis 6(5) (2000) 437-444.

[28] A.Y. Gerard, J. Han, S.J. McDonnell, K. Oglec, E.J. Kautz, D.K. Schreiber, P. Lu, J.E. Saal, G.S. Frankel, J.R. Scully, Acta Materialia in-press (2020).

[29] K. Wang, J. Han, A.Y. Gerard, J.R. Scully, B.-C. Zhou, npj Materials Degradation under review (2020).

[30] F. Gesmundo, P. Nanni, D.P. Whittle, Corrosion Science 19(10) (1979) 675-691.

[31] K.-Y. Tsai, M.-H. Tsai, J.-W. Yeh, Acta Materialia 61(13) (2013) 4887-4897.

[32] Y. Unutulmazsoy, R. Merkle, J. Mannhart, J. Maier, Solid State Ionics 309 (2017) 110-117.

[33] C. Desgranges, F. Lequien, E. Aublant, M. Nastar, D. Monceau, Oxidation of Metals 79(1) (2013) 93-105.

Graphical Abstract

Formation of a layered oxide comprised of a Cr-rich inner layer, Cr-poor outer layer. All cations are found in the oxide.